Inorganic Chemistry
Cite This: Inorg. Chem. 2019, 58, 11738–11750
Article
pubs.acs.org/IC

Joint Theoretical and Experimental Study on the La Doping Process in In_2O_3: Phase Transition and Electrocatalytic Activity

S. C. S. Lemos,[†] E. Nossol,[†] J. L. Ferrari,[†] E. O. Gomes,[‡] J. Andres,[‡] L. Gracia,[‡] I. Sorribes,[‡] and R. C. Lima*[,†]

[†]Instituto de Química, Universidade Federal de Uberlândia, 38400-902 Uberlândia, Minas Gerais, Brazil
[‡]Departament de Química Física i Analítica, Universitat Jaume I, 12071 Castellón, Spain

Supporting Information

ABSTRACT: In_2O_3 and La^{3+}-doped In_2O_3 nanostructures were synthesized through a facile and fast chemical route based on the microwave-assisted hydrothermal method combined with rapid thermal treatment in a microwave oven. The presence of the La^{3+} doping process modifies the size and morphology of the In_2O_3 nanostructures and also stabilizes the rhombohedral (rh) In_2O_3 phase with respect to the most stable cubic (bcc) polymorph. X-ray diffraction (XRD) patterns and Rietveld refinements, Raman, UV−vis, and energy dispersive X-ray (EDX) spectroscopies, transmission electron (TEM) and field-emission scanning electron (FE-SEM) microscopies, as well as PL emissions have been performed. To complement and rationalize the experimental results, first-principle calculations, based on density functional theory, are carried out to obtain the formation energies of the In_2O_3 and bcc- and rh-In_2O_3-doped phases, their geometry and electronic properties. Theoretical results are able to explain the relative stabilization of the rh-phase with respect to the bcc-phase based on the analysis geometry changes and the electronic redistribution induced by the La^{3+} doping process. In addition, Wulff construction is employed to match the theoretical and experimental morphologies of the cubic phase. The synthesized samples were applied for the O_2 evolution reaction (OER). The La^{3+}-doped In_2O_3 film presents superior electrocatalytic activity, with an onset potential lower than the undoped In_2O_3 film that can be associated with the increase in electron density caused by the La^{3+} doping process. This study provides a versatile strategy for obtaining In_2O_3 and La^{3+}-doped In_2O_3 nanostructures for practical applications.

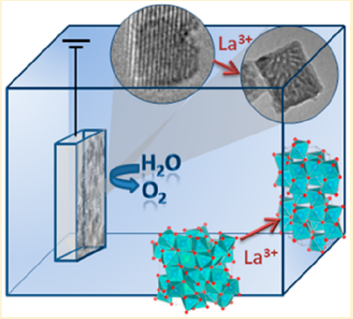

1. INTRODUCTION

Electrochemical and photochemical water splitting have been addressed as a promising and sustainable technology for energy conversion. These processes involve two half-reactions: water oxidation (or the oxygen evolution reaction (OER)) and water reduction (or the hydrogen evolution reaction (HER). The OER, requiring four proton and electron transfers per oxygen molecule, is the more complex of the two half-reactions; consequently, it limits the overall water-splitting process.[1−4] To overcome this issue, semiconductor-based catalysts meeting the band gap requirement and having a valence band below the O_2/H_2O level have been developed with the aim of improving the OER.[5,6] In this type of material, the oxidation of water is promoted by holes generated in the interface of the n-type semiconductor and the electrolyte.[6,7]

Indium oxide (In_2O_3) is a wide-band n-type semiconductor, even in the absence of intentionally added donors,[8] which satisfies the band edge position requirement for water electrolysis. In addition, the presence of defects such as oxygen vacancies or the presence of dopants allows for the possibility of decreasing the electron/hole recombination and increasing the interfacial electron transfer process.[9] Concerning the other defects generated due to reducing different aspects of the conditions that have a real and relevant impact on the catalytic activity of reduced In_2O_3, Gu et al.[10] varied the oxygen vacancies content in order to find the optimal proportion for sensing properties by varying the hydrogen annealing time. Davies et al.[11] explored the features of formation of In^+ in the In_2O_3 surface under reducing conditions by combining X-ray photoemission measurements with first-principles density functional theory (DFT) calculations.

In_2O_3 offers a wide range of applications such as transparent electronics,[12] sensors,[13,14] photovoltaic devices,[15] light-emitting diodes,[16] solar cells,[17] and gas sensors.[18,19] In this context, the study of the surface structure and defects, electron accumulation, and control of vacancies and carrier density that directly affect the material efficiency is mandatory.[20,21] In_2O_3 can crystallize in a cubic and/or rhombohedral polymorphic form.[22] The body centered cubic structure (bcc-In_2O_3) is the most stable with lattice constants $a = b = c = 10.118$ Å, in which each In^{3+} cation is situated in the center of a distorted cube with only six vertices occupied by oxygen anions, while the remaining two vertices are empty.[23] The metastable rhombohedral polymorph (rh-In_2O_3) is obtained at high temperatures and pressures, with lattice parameters of $a = b = 5.478$ Å and $c = 14.510$ Å, and in this arrangement, the In^{3+} cations are coordinated octahedrally with two layers of oxygen anions.[24] The process of phase trans-

Received: June 10, 2019
Published: August 15, 2019

DOI: 10.1021/acs.inorgchem.9b01728
Inorg. Chem. 2019, 58, 11738−11750

formation in In_2O_3 has been a focus of attention, since the different polymorphs show specific properties that directly affect the performance of the desired applications.[25] Koch et al.[26] observed from adsorption measurements that rh-In_2O_3 exhibits predominantly Lewis acidic surface sites compared to bcc-In_2O_3; thus, the cubic structure presented a superior CO_2 selectivity in methanol steam reforming. Wu et al.[27] investigated the photocatalytic activities of rh-In_2O_3 and bcc-In_2O_3 nanostructures and obtained the highest efficiency for degradation of tetracycline using rh-In_2O_3. Furthermore, In_2O_3 with coexisting cubic and rhombohedral phases showed improved performance for NO_2 sensing, with excellent selectivity and stability.[28]

The dopant processes in the oxide matrix are a useful approach to design the material properties, such as band gap engineering, morphology control, and changing the electrical carrier density.[29−32] Studies addressing the doping effect in an In_2O_3 host have been carried out, such as the work of Xu et al.,[30] who proposed a selection of suitable transition metals as dopants to achieve higher carrier density and optical transparency. In this context, Farvid et al.[33] evaluated the effect of Cr^{3+} doping on In_2O_3 host lattice, attributing the stabilization of the metastable rh-In_2O_3 phase to the inhibition of the nanoparticles growth due to the presence of dopant ions in the reaction mixture, while Li et al.[28] showed the dependence of the phase transition process and morphology transformation provoked by the dopant concentration in Zn-doped In_2O_3. Very recently, our group has successfully synthesized In_2O_3 and Er^{3+}-doped In_2O_3 nanostructures, and their PL emissions and photocatalytic activities have been investigated.[34−36] Doping processes involving rare earth elements have been proposed as a route to control the size, morphology, and even the stabilization of a specific crystallographic phase.[37−41] In particular, La^{3+} is known to perform a crucial role in advanced photocatalytic technologies. For instance, Zhang et al. reported the presence of a higher density of oxygen vacancies due to the La^{3+} doping process in TiO_2, and consequently, an improvement in photoelectric conversion efficiency was achieved. Oppong et al.[42] reported a decrease in the electron hole recombination in ZnO due to empty 4f and 5d orbitals of La^{3+}, and Wei et al.[43] achieved a higher performance for H_2S sensing due to an improved ability to adsorb the ionized oxygen species on the In_2O_3 surface throughout the La^{3+} doping process.

In the present work the microwave hydrothermal-assisted method was combined with a calcination process performed in a microwave oven.[44−48] This annealing treatment has the advantage of reducing the temperature and the calcination time,[34−36] which in this work yielded the formation of well crystallized In_2O_3 within 2 min of calcination. Adequate synthesis methods coupled with a detailed electronic and structural description of In_2O_3 promote an understanding of the fundamental knowledge to be applied for the development of the functionalities of this material. Inspired by the above-mentioned studies, herein we seek to accomplish four aims. First, we report a simple and efficient method to efficiently fabricate both In_2O_3 and La^{3+}-doped In_2O_3 by employing a microwave-assisted route. Second, the effects of the La^{3+} dopant in the phase formation (rh-In_2O_3 vs bcc-In_2O_3) have been analyzed. To support these findings, X-ray diffraction and Rietveld refinements, energy dispersive X-ray (EDX), Raman, and UV−vis spectroscopies, as well as PL emissions have been studied. The structures of the two phases have been investigated by first-principle calculation, based on DFT, to obtain their relative stabilities and structure differences at the atomistic level. In addition, from the analysis of the theoretical results, we disclose the mechanism through which the La doping process stabilizes more of the rh-In_2O_3 with respect to bcc-In_2O_3. The third objective is to explain how the theoretical and experimental morphologies from FE-SEM images of the cubic phase are rationalized based on the Wulff construction by first-principle calculations. Finally, the fourth objective is to demonstrate that the prepared In_2O_3 and La^{3+}-doped In_2O_3 films present electrocatalytic activity for water oxidation and contribute to broaden their possible applications.

2. EXPERIMENTAL AND THEORETICAL METHODS

2.1. Synthesis. The precursors were obtained from the addition of 14.40 mL of an $In(NO_3)_3$ solution (0.10 mol L^{-1}) and 2.00 mL of PEG 200 in 40 mL of distilled water under constant stirring. The pH was adjusted to 9.70 using a KOH aqueous solution (3.0 mol L^{-1}). To prepare the doped precursor, a stoichiometric amount of a $La(NO_3)_3$ solution (0.20 mol L^{-1}) was added to the mixture in order to reach a concentration of 4.0 mol % La^{3+} in relation to In^{3+} ions. The final solution was transferred into an autoclave, sealed, and placed in the microwave-hydrothermal equipment. The solutions were heated at 140 °C for 2 min, employing a heating rate of 5 °C min^{-1}. The precipitate powder was washed several times with deionized water and ethanol and dried at 60 °C for 3 h. The as-prepared $In(OH)_3$ and La^{3+}-doped $In(OH)_3$ precursors were annealed at 350 °C for 2 min in a microwave oven to obtain In_2O_3 nanostructures.

2.2. Characterization Techniques. The In_2O_3 powders were characterized by X-ray diffraction (Shimadzu XRD 6000) using Cu Kα as the radiation source. The structure was refined using the Rietveld method and the General Structure Analysis System (GSAS) package, with the EXPGUI graphical user interface.[49] The cubic and rhombohedral structures of In_2O_3 were generated using the Crystal Maker program (Version 2.2.4.445) for Windows. The morphological characterization was carried out using a field-emission scanning electron microscope (FE-SEM, Zeiss Supra35) operating at 5 kV. Transmission electron microscopy (TEM) was carried out on a FEI Tecnai G2F20, operating at 200 kV. The microanalysis by energy dispersive X-ray (EDX) spectroscopy was carried out using an Oxford Instruments system, operating at 20 kV. UV−visible spectra were obtained on a Cary 5G spectrophotometer in the region 200−900 nm. Raman spectra at room temperature were recorded on an RFS/100/S Bruker FT-Raman spectrometer, with an Nd:YAG laser providing an excitation light at 1064 nm and a spectral resolution of 4 cm^{-1}. Photoluminescence (PL) spectra were recorded at room temperature by a thermal Jarrel-Ash Monospec 27 monochromator and a Hamamatsu R446 photomultiplier (λ_{exc} = 350.7 nm).

2.3. Electrochemical Studies. To carry out the electrochemical studies, undoped and doped In_2O_3 with 4.0 mol % La^{3+} films were prepared based on the interfacial method.[50,51] For this purpose, 3.0 mg of the In_2O_3 powder were added to 20 mL of water, vigorously stirred for 30 min, and maintained in an ultrasonic bath for further 30 min. Then, the resulting dispersion was transferred to a 50 mL round-bottomed flask containing 20 mL of toluene. The two-phase system was maintained under strong magnetic stirring for 24 h. Then, the magnetic stirring was stopped, and the transparent film obtained on the interface was deposited onto the ITO surface (sheet resistance of 9−15 ohm/sq and thickness of 180 nm), and dried at 70 °C for 2h.

Cyclic voltammetry (CV) was carried out using a PGSTAT12 Autolab potentiostat equipped with a conventional one-compartment, three-electrode cell containing the nanostructured film as the working electrode, a platinum wire as the counter electrode, and Ag/AgCl (3.0 mol L^{-1} KCl) as the reference electrode. Electrocatalytic activity for water oxidation was measured in a 0.1 mol L^{-1} phosphate buffer with the addition of a 3 mol L^{-1} KOH solution for pH adjustment. CV of the electrode was obtained at a scan rate of 50 mV s^{-1}.

2.4. Computational Methods and Model Systems. First-principles calculations within the periodic DFT framework, using the hybrid B3LYP exchange−correlation functional, were performed with

DOI: 10.1021/acs.inorgchem.9b01728
Inorg. Chem. 2019, 58, 11738−11750

the CRYSTAL17 program[52] to characterize the In_2O_3 and La^{3+}-doped In_2O_3 systems. All-electron basis sets were used to describe O[53] atomic centers, a pseudopotential basis set for the In atom,[54] and an effective core potential (ECP) pseudopotential with 11 valence electrons described was used for the La^{3+}.[53] Regarding the density matrix diagonalization, the reciprocal space net was described by a shrinking factor of 4, corresponding to 36 k-points generated according to the Monkhorst−Pack scheme. The accuracy of the evaluation of the Coulomb and exchange series was controlled by five thresholds, whose adopted values were 10^{-8}, 10^{-8}, 10^{-8}, 10^{-8}, and 10^{-16}. A supercell of 80 atoms, corresponding to 2 × 2 × 1 conventional cells, was used to simulate the La^{3+}-doped In_2O_3 systems. A 12.50% substitution of In^{3+} ions by La^{3+} cations was performed in order to match the experimental value in which the rh-phase of In_2O_3 was formed.

In addition, the surface energies, E_{surf}, of the (100), (110), (111), and (211) surfaces were calculated for the cubic phase by using the Wulff construction, which minimizes the total surface free energy at a fixed volume, providing a simple correlation between the surface energy of the (hkl) plane and the distance (r_{hkl}) in the normal direction from the center of the crystallite.[55] The procedure to obtain the complete set of morphologies, based on the Wulff construction and the surface energy, has been previously presented by Andrés et al.[56] and it has been successfully used in materials science to obtain the morphology of materials, including $PbMoO_4$, $CaWO_4$, Ag_3PO_4, α-Ag_2MoO_4, $BaMoO_4$, $BaWO_4$, Ag_2CrO_4, and $LaVO_4$.[57−64] The surface energy (E_{surf}) is defined as the total energy per repeating slab cell (E_{slab}) minus the total energy of the perfect crystal per molecular unit (E_{bulk}/atom) multiplied by the number of molecular units of the surface (N) and divided by the surface area per repeating cell of the two sides of the slab: $E_{surf} = 1/2A(E_{slab} - N{\cdot}E_{bulk})$.

A schematic representation of the unit cell of bcc-In_2O_3 (a) and rh-In_2O_3 (b) structures are presented in Figure 1a,b, respectively. The In^{3+} cations in the bcc-In_2O_3 structure occupy two nonequivalent positions, 8b and 24d according to the Wyckoff notation, surrounded by oxygen anions in the octahedral and trigonal prismatic coordination, [InO_6] cluster, respectively.

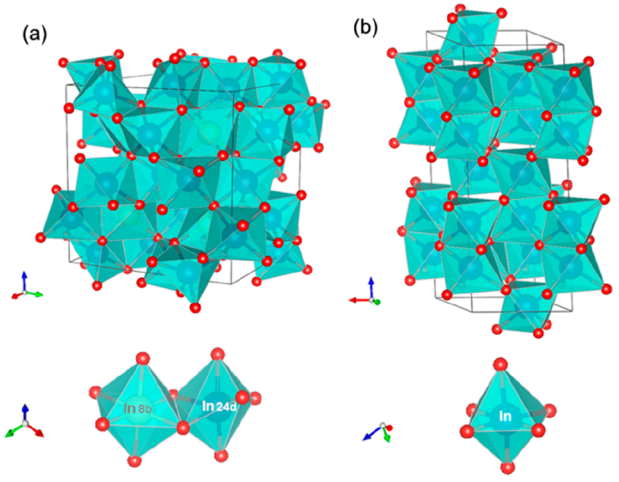

Figure 1. Schematic representation of the unit cells of (a) bcc-In_2O_3 and (b) rh-In_2O_3 structures.

3. RESULTS AND DISCUSSION

The $In(OH)_3$ and La^{3+}-doped $In(OH)_3$ precursors were obtained by a microwave synthesis at 140 °C for 2.0 min under hydrothermal conditions. The X-ray diffractograms of the precursors are shown in Figure 2a. For all samples, diffraction peaks regarding the cubic structure of indium hydroxide were indexed according to Powder Diffraction File (PDF) no. 85−1338 (Joint Committee on Powder Diffraction Standards (JCPDS), [1967]). The presence of a second phase is perceived due to the peaks at 25.9 and 33.7° for the La^{3+}-doped sample, corresponding to the orthorhombic structure of the indium oxyhydroxide (InOOH) according to PDF no. 17−0549 (JCPDS, [1964]). The short reaction time in the preparation of these materials indicates the efficiency of the microwave hydrothermal method for obtaining $In(OH)_3$ nanoparticles and the incorporation of the La^{3+} ions into the hydroxide lattice.

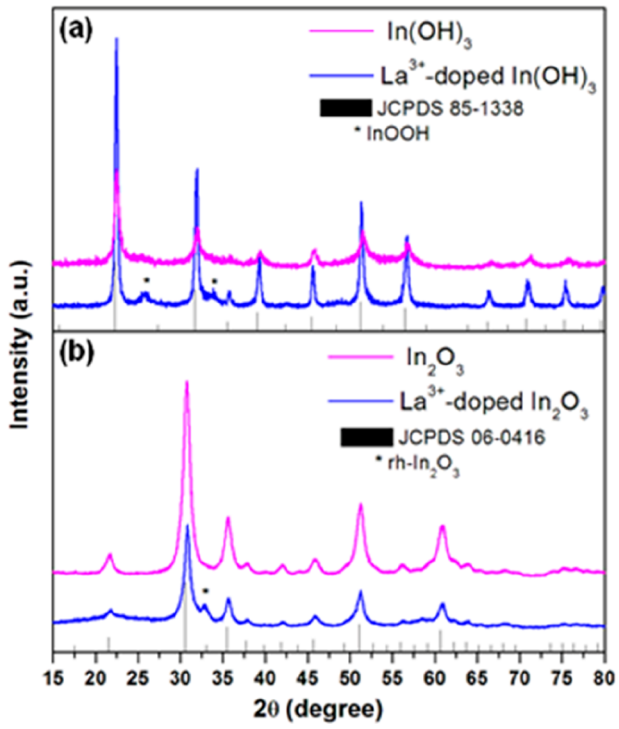

Figure 2. XRD patterns of the as-synthesized In_2O_3 and La^{3+}-doped $In(OH)_3$ (a) and of the In_2O_3 and La^{3+}-doped In_2O_3 obtained after calcination (b). PDF nos. 85−1338 and 06−0416 (JCPDS, [1967 and 1955, respectively]).

In order to obtain In_2O_3 and La^{3+}-doped In_2O_3 materials, the $In(OH)_3$ precursors were subjected to microwave oven calcination at 350 °C for 2 min. The corresponding XRD patterns are shown in Figure 2a. It was observed that a single cubic phase bcc-In_2O_3 was formed for the undoped In_2O_3 sample, in accordance with crystallographic data card PDF no. 06−0416 (JCPDS, [1955]). The diffractogram of the La^{3+}-doped In_2O_3 sample shows, in addition to the peaks of the bcc-In_2O_3 structure, a peak at 2θ = 32.63° corresponding to the plane (110) of the rhombohedral phase rh-In_2O_3, according to PDF no. 72−0683 (JCPDS, [1969]). An analysis of the results displayed in Figure 2b shows that a mixture of bcc and rh-In_2O_3 is presented; the addition of La^{3+} cations in the structure of In_2O_3 triggers the appearance of the (110) peak of the rhombohedral phase, rh-In_2O_3.

A Rietveld refinement method was performed for the In_2O_3 and La^{3+}-doped In_2O_3 samples, as shown in Figure 3. In Table 1 the values of the profile and lattice parameters obtained after the final refinement cycle are presented. The low values of χ^2 and the profile parameters (R_p, R_{wp}) indicate a high quality of refinement. The presence of the dopant influences phase formation, wherein the undoped bcc-In_2O_3 was transformed into a mixture of bcc-In_2O_3 and rh-In_2O_3. Rietveld refinement of the XRD patterns of the La^{3+}-doped In_2O_3 sample renders the

DOI: 10.1021/acs.inorgchem.9b01728
Inorg. Chem. 2019, 58, 11738−11750

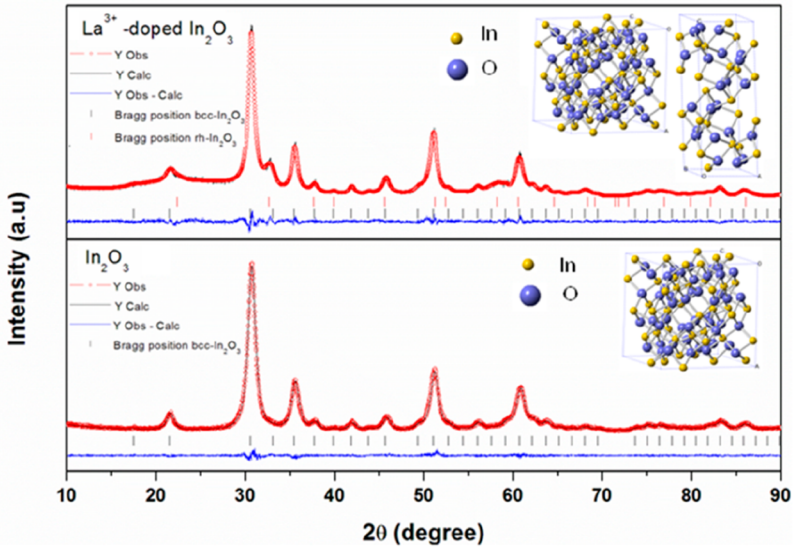

Figure 3. Rietveld refinement of XRD patterns for the In_2O_3 and La^{3+}-doped In_2O_3 samples. The respective crystal structures obtained from Rietveld refinements, comprising the cubic and rhombohedral phases, are shown in the upper right corner.

Table 1. Quality and Parameters Obtained by the Rietveld Method for the In_2O_3 Samples

	bcc-In_2O_3 cell parameters	rh-In_2O_3 cell parameters						
	$a = b = c$ (Å)	$a = b$ (Å)	c (Å)	rh phase fraction (%)	R_{wp} (%)	R_p (%)	R_{Bragg} (%)	χ^2
In_2O_3	10.1110(3)				6.23	4.65	1.09	1.191
La^{3+}-In_2O_3	10.1202(5)	5.4842(11)	14.5053(10)	19.7	6.31	4.98	1.63	1.459

presence of 80.3% bcc-In_2O_3 phase and 19.7% rh-In_2O_3. The cubic and rhombohedral structures of In_2O_3 samples were generated from the Rietveld refinement data and are represented in the inset of Figure 3.

In the present work, we observed that the La^{3+} doping process promotes the formation of the rh-In_2O_3 phase to a larger extent with respect to the Er^{3+} doping process, reported in our previous work.[36] A comparison of the results obtained from the Rietveld refinement shows that a percentage of 19.7% was achieved for the rh-In_2O_3 phase with La^{3+} doping and 12.7% with the Er^{3+} one. This result was also observed by Wang et al.,[65] in which the influence of La^{3+} doping on the crystal phase can be related to size and dipole polarizability of the substitutional dopant. The La^{3+} cation has a larger ionic radius than the Er^{3+} cation, exhibiting a greater tendency toward the distortion of the electronic cloud, thus favoring even more the formation of the rh-In_2O_3 phase.

The La^{3+} doping at both 8b and 24d sites modifies the distortion of the octahedral coordination due to mismatch in ionic radii of $La^{3+}$and In^{3+}cations. To gain further insight into the source of the relative stabilization of the rh-In_2O_3 phase with respect the bcc-In_2O_3 induced by the La^{3+} doping process, first-principles calculations were carried out to study the La^{3+}-doped In_2O_3 crystal structure at different amount of La^{3+}-doping (3.1, 9.3, and 12.5 mol %) for both phases (rh- and bcc-In_2O_3) and for the two Wyckoff positions. First, it was found that the substitution of In^{3+} by La^{3+} in the bcc-In_2O_3 structure is more energetic at the d site, 1.97×10^{-4} Hartree.

An analysis of the results presented in Table 2 shows that the undoped bcc-In_2O_3 phase is more stable than the rh-In_2O_3 one; however, as the percent of La^{3+} doping content increases, the rh-phase is stabilized with respect to the bcc-structure. Substituting In^{3+} by La^{3+} cations in both positions 8b and 24d achieves an

Table 2. Calculated Cell Parameters, a and c (Å) and the Energy Difference $E_{bcc} - E_{rh}$ (Hartree) between bcc and rh Structures of the In_2O_3 and La^{3+}-In_2O_3 Structures at Different % of La^{3+} Doping[a]

	bcc	rh		
In_2O_3	a	a	c	$E_{bcc} - E_{rh}$
undoped	10.123	5.474	14.585	−0.0071
3.1% La^{3+} (8b)	11.104	5.489	14.624	−0.0062
3.1% La^{3+} (24d)	11.078			−0.0064
9.3% La^{3+} (8b)	11.220	5.514	14.691	−0.0021
9.3% La^{3+} (24d)	11.180			−0.0022
12.5% La^{3+} (8b)	11.298	5.525	14.720	0.0010
12.5% La^{3+} (24d)	11.298			0.0393

[a]Cell parameters referred to a single unit cell. E_{bcc} = −229.73034 hartree. 8b and 24d refer to the Wyckoff positions of bcc-In_2O_3.

energy in which the rh-In_2O_3 phase is more stable than the bcc-In_2O_3 phase when the doping percentage reaches the value of 12.5% at both 8b and 24d positions.

An analysis of the values of the In−O and La−O bond distances at the [InO_6] and [LaO_6] clusters, i.e., the local coordination of both In^{3+} and La^{3+} at both undoped and doped bcc- and rh-In_2O_3 structures (see Tables S1 and S2) renders that the substitution of In^{3+} by La^{3+} provokes an expansion of the clusters due to the large ionic radius of La^{3+} with respect to In^{3+}, i.e., the La−O bonds are larger than In−O for both bcc- and rh-In_2O_3 phases. However, it is interesting to note that [LaO_6] clusters display a more remarkable structural distortion in the rh-In_2O_3 phase at 12.5% La content of the rh-In_2O_3 phase, with four different La−O distances.

Furthermore, the value O−In(8b)−O bond angle decreases from 87.5 to 80.6° in 12.5% La^{3+}-doping for the bcc-phase, while

DOI: 10.1021/acs.inorgchem.9b01728
Inorg. Chem. 2019, 58, 11738−11750

the other O−In(8b)−O bond angle increases from 93.3 to 98.8°; for the O−In(24d)−O bond angle, their values decrease from 78.5 to 76.3°, and increases from 98.3 to 104.0° on going from the bcc-phase to 12.5% amount of La^{3+} doping. The values of the O−La−O bond angles at bcc- and rh-phase for the same doping percentage are 77.0 and 103.0°, as well as 73.5 and 110.0°, respectively (see Table S3). These values indicate that the geometry of the rh phase has more flexibility than the bcc phase to carry out the La^{3+}-doping process, demonstrating that the [LaO_6] octahedra in the rh-doped structure has more liberty to expand and rotate. This fact indicates that the rh-In_2O_3 structure is more prone to accept the substitution of La^{3+} that entails larger structural distortion with a lower energy cost. These theoretical results are able to explain the experimental findings, i.e., the formation of the rh-In_2O_3 phase is promoted when In^{3+} is replaced by La^{3+} cations. Overall, the structural deformations at the lattice of the rh- and bcc-In_2O_3 arise due to two types of distortions: One is due to tilting of InO_6 octahedra, and the other results from the length asymmetry in six In−O bonds surrounding the In^{3+} cation in the [InO_6] octahedra. Considering the above observation, it is easy to realize that such structural order−disorder modifications provoked by the La^{3+} doping process is more favorable at rh than bcc phase of In_2O_3. This behavior was also found on a study based of $NaYF_4$ doped with light lanthanides, where hexagonal phase is favored compared to cubic one.[65]

The FE-SEM images of the In_2O_3 and La^{3+}-doped In_2O_3 samples are displayed in Figure 4a,b and consist of agglomerated

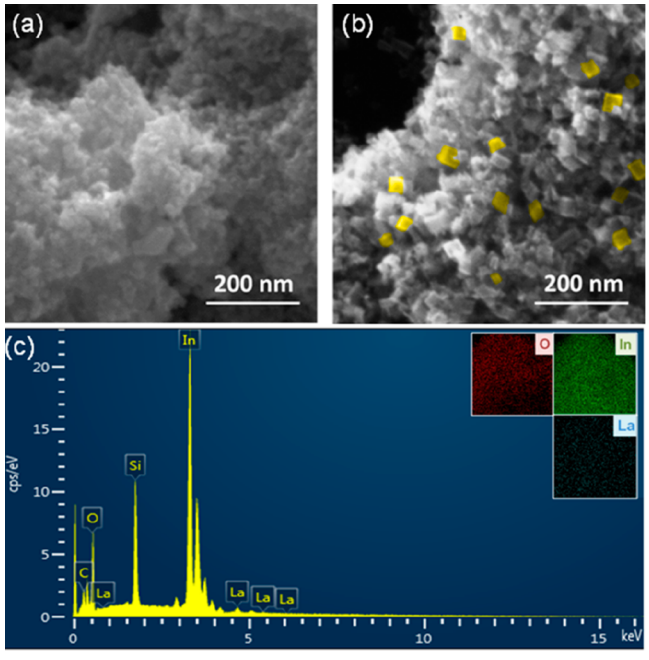

Figure 4. FE-SEM images of: In_2O_3 (a), La^{3+}-doped In_2O_3 (b), and EDX of the La^{3+}-doped In_2O_3 sample (c). The inset in (c) represents the elemental mapping of the La^{3+}-doped In_2O_3 sample.

formation and larger size cubic shaped nanoparticles, respectively. The growth process and morphology of the final nanoparticles depend on the degree of saturation of the reaction medium, the diffusion rate of the species present on the surface of the crystals and, consequently, on the interfacial energies involved in the process.[66] From the results obtained, it is clear that the presence of La^{3+} affects the morphology and size of the synthesized particles.

The presence of La^{3+} in the doped sample is confirmed by the EDX spectrum (Figure 4c). The elemental mapping of the La^{3+}-doped In_2O_3 sample is presented in the inset of Figure 4c, showing uniform distributions of the In, O, and La elements at the surface of the nanostructures.

From the thermodynamic point of view, the shape of crystals grown under a real or near equilibrium condition is dominated by the energies of the different surfaces. The (110), (100), (111), and (211) surfaces of the bcc-In_2O_3 phase were modeled using slab models with the calculated equilibrium geometries. According to the DFT calculations, the stability of the surfaces follows the order (100) < (211) < (110) < (111), with surface energies of 3.62, 2.29, 1.40, and 1.02 J m^{-2}, respectively. Since the coordination environment affects the stabilization of the surfaces, the higher stability of the (111) surface is attributed to the presence of [InO_6] clusters in the exposed surface, while for the other surfaces, the presence of oxygen vacancies in the superficial and undercoordinated In clusters increases the value of the surface energy (Figure S1). An analysis of the theoretical results reveals that the most stable morphology is an octahedron, in which only the (111) surface appears. From the energy obtained using the slab models, it is possible to modulate the surface energies to find the morphology obtained experimentally. This strategy is based on the fact that the morphology is derived from calculated surface energies using the assumption that crystal faces with the lowest surface energies control the final crystal morphology. Therefore, different possible morphologies can be obtained by increasing or decreasing the stability of the different facets. A truncated octahedron can be obtained if the surface energy of (110) is decreased to 0.80 J m^{-2}, while a truncated sphere can be produced when the surface energy of (211) is decreased to 0.50 J m^{-2} (see Figure 5).

The experimentally obtained morphology of the La^{3+}-doped In_2O_3 sample makes possible to find the path that is capable of matching the theoretical morphology. This agreement is obtained when the values of the surface energy for (100) decrease to 0.30 J m^{-2}, where the presence of La^{3+} cations in the In_2O_3 matrix lower the (100) surface energy, and thus the cubic shape is able to appear (see Figure 5). This behavior was emphasized by Cho et al.,[67] where the presence of foreign ions in the reaction environment can drive the surface energy toward the formation of a specific morphology; in particular, a well-defined cubic morphology was achieved with fluorine doping. These authors evaluated the energies of F-substitution at the surface of In_2O_3, showing that the surface binding of F atoms directs the stabilization of the (100) facets.

The analysis of the TEM images reveals a difference in the morphology of In_2O_3 and La^{3+}-doped samples. The undoped In_2O_3 sample presents smaller particles, with a size of around 8 nm and irregular shapes (Figure 6a), while the La^{3+}-doped In_2O_3 sample shows an increased size and a verified cubic morphology (Figure 6b). As can be seen in Figure 6c,d, HRTEM images of the In_2O_3 sample show the (222) lattice spacing (2.91 and 2.98 Å). For La^{3+}-doped In_2O_3, the (400) lattice spacing (2.59 Å), (211) lattice spacing (4.16 Å), and, from the rhombohedral phase, the (110) lattice spacing (2.77 Å) can also be observed (Figure 6e,f). These results indicate that the La^{3+} doping allows to access other surface facets beyond the (111), observed for the undoped In_2O_3.

The Raman spectra obtained is presented in Figure 7a. The body-centered cubic structure In_2O_3 (bcc-In_2O_3) belongs to

DOI: 10.1021/acs.inorgchem.9b01728
Inorg. Chem. 2019, 58, 11738−11750

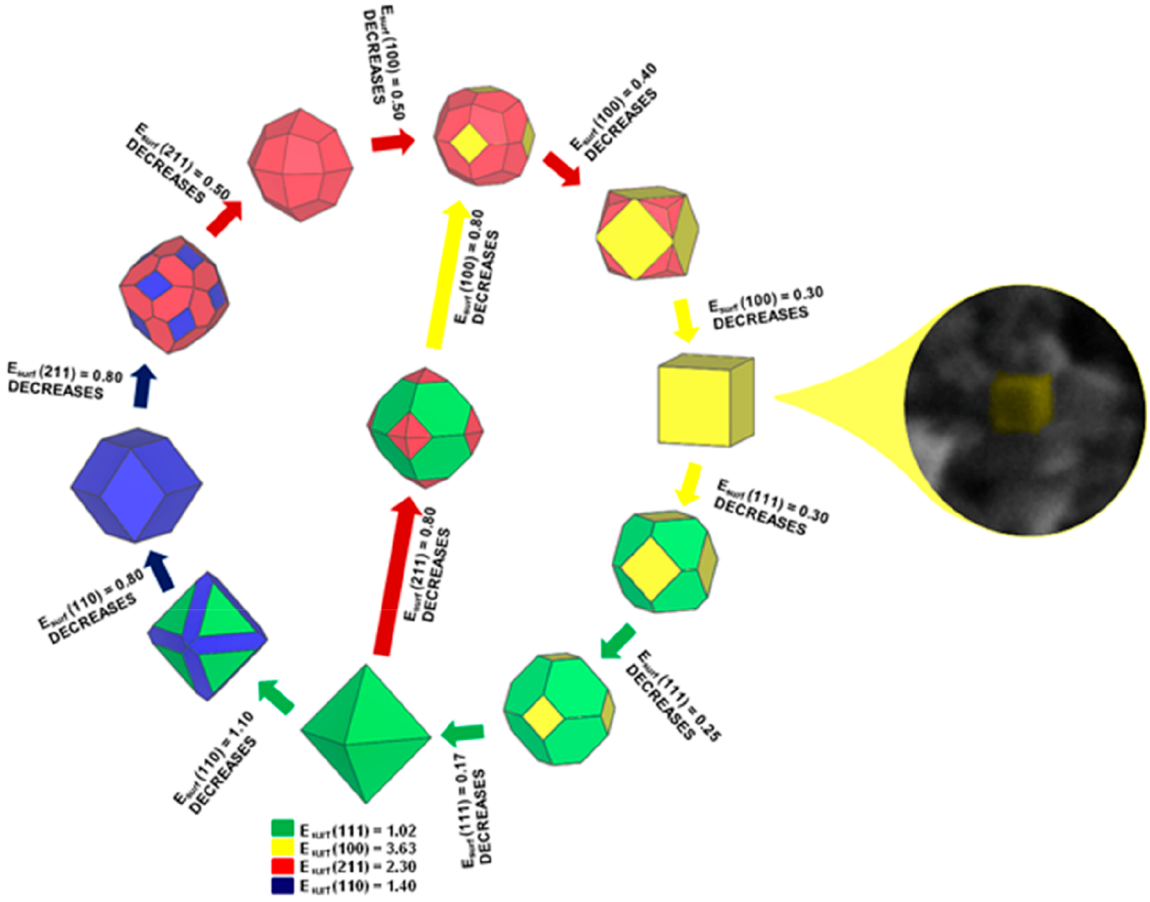

Figure 5. Map of the morphologies of bcc-In_2O_3 taking into account (100), (110), (111), and (211) surfaces (with surface energy expressed in J m^{-2}). An image of the In_2O_3 cube-form particle obtained from SEM is shown on the right.

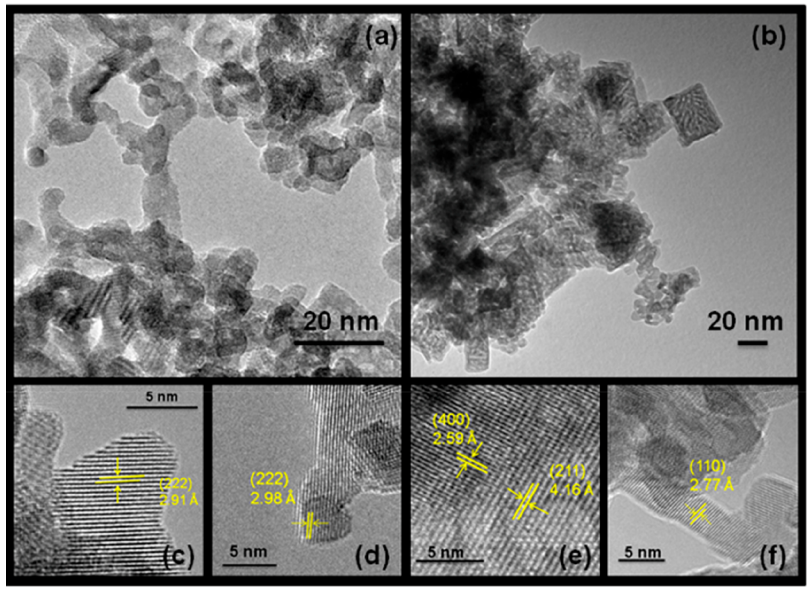

Figure 6. TEM images of In_2O_3 (a) and La^{3+}-doped In_2O_3 nanostructures (b). HR-TEM images of In_2O_3 (c, d) and La^{3+}-doped In_2O_3 nanocrystals (e, f).

space group $Ia\bar{3}$, T_h^7. For this structure, among the following predicted modes ($4A_g + 4E_g + 14F_g + 5A_u + 5E_u + 16T_u$), only A_g, E_g, and F_g are Raman active.[68] The Raman spectra of the In_2O_3 and La^{3+}-doped In_2O_3 samples display characteristic bands of the vibration modes of body-centered cubic oxide, which agree with values reported in the literature.[69,70] The main signals for the synthesized samples were observed at 131 cm^{-1} (A_g^1), which is related to In−O (vibration of InO_6 structure units) at 308 cm^{-1}, attributed to the bending vibration of the InO_6 octahedron (superposition of the F_{2g}^4 and A_g^3 modes), and

DOI: 10.1021/acs.inorgchem.9b01728
Inorg. Chem. 2019, 58, 11738−11750

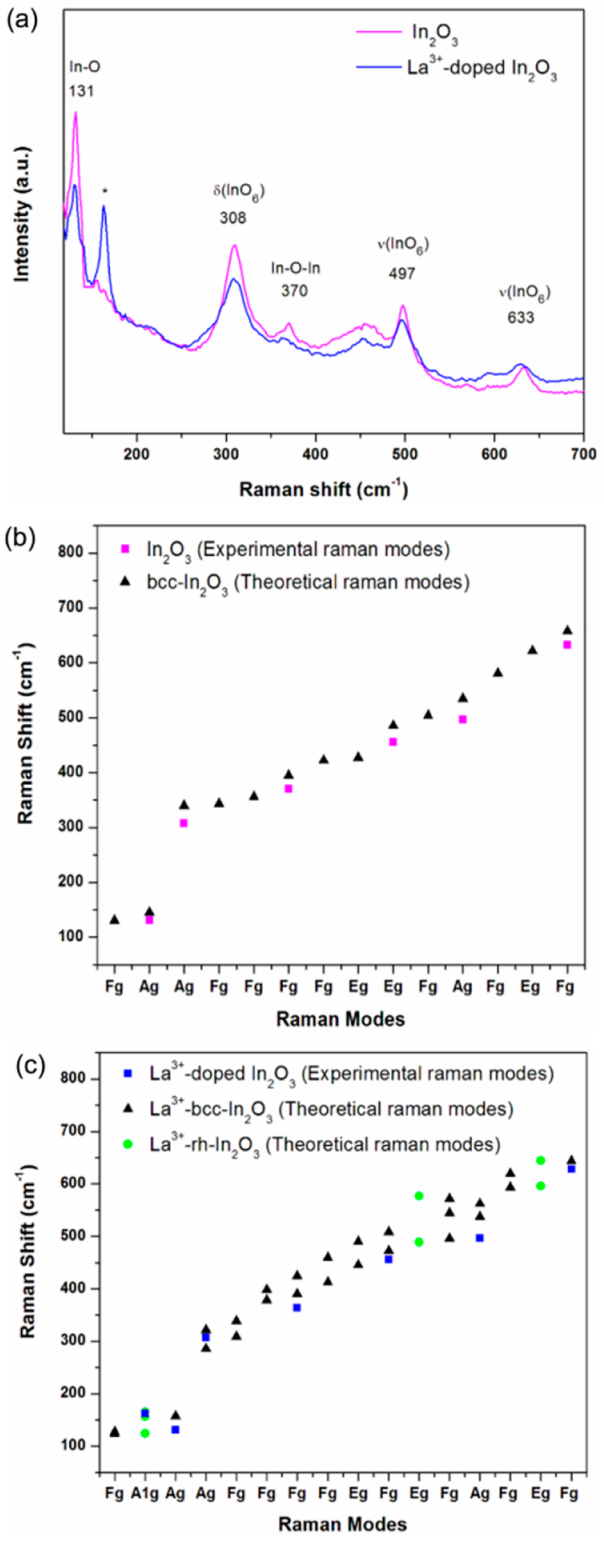

Figure 7. Raman spectra of In_2O_3 and La^{3+}-doped In_2O_3 samples (a) and comparison between the positions of theoretical and experimental Raman-active modes bcc-In_2O_3 (**b**) and rh-In_2O_3 (**c**).

a signal at 370 cm^{-1}, which is due to stretching vibrations of In−O−In (F_{2g}[5]). The bands at 497 and 633 cm^{-1} are also assigned to the stretching vibrations of the InO_6 octahedrons.

The rh-In_2O_3 structure belongs to the space group $R\bar{3}c$, D_{3d}^6. The irreducible representation of the optical modes for the crystal are $2A_{1g} + 2A_{1u} + 3A_{2g} + 2A_{2u} + 5E_g + 4E_u$, of which only the vibrations with symmetry A_{1g} and E_g are active in Raman spectroscopy.[70] The Raman spectra of La^{3+}-doped In_2O_3 presents a strong band at 162 cm^{-1}, attributed to the A_{1g} symmetry of rh-In_2O_3, indicating the coexistence of cubic and rhombohedral phases of In_2O_3, which is in agreement with the X-ray diffraction characterization.

Furthermore, the vibration of the In−O−In bond is known to be affected by the presence of oxygen vacancies.[9] The relative intensity and shift of the Raman band position can reflect the density of defect states of oxygen.[71−73] The observed redshift of the In−O−In mode to 363 cm^{-1} for the La^{3+}-doped sample can be attributed to the weaker bond strength forces due to the La^{3+} insertion.

A comparison of theoretical and observed experimental positions of the Raman active modes is presented in Figure 7b,c, respectively. An analysis of the results revealed a good agreement between the Raman shifts (cm^{-1}) of the experimental modes compared to the theoretical modes for the bcc-In_2O_3 structure. The insertion of La^{3+} cations gives rise to a change in the crystal lattice with concomitant variations in the position of the Raman modes, as can be observed in Figure 7c. The bands presented in the host matrix spectrum are affected by the dopant, since the Raman bands arising from the vibrational modes that involve a significant contribution of atomic motion from the dopant atom may exhibit a shifting of the peak position (Tables S4 and S5). In addition, since the structural disorder within the undoped In_2O_3 and the La^{3+}-doped In_2O_3 compounds loses its translational symmetry, Raman spectroscopy can be used to investigate the nearest-neighbor changes in these structures. Disordering allows more phonons to contribute to the optical spectra, thus causing a general broadening of all the Raman active modes.

The values of the band gap of each sample were calculated by linear extrapolation of the curve using the method proposed by Kubelka−Munk[74] from absorption spectra in the visible region (Figure S2). The estimated band gap values are 2.9 eV for the undoped In_2O_3 sample, which presents only the bcc phase, and 3.2 eV for the sample doped with 4.0 mol % of La, presenting a mixture of bcc and rh phases.

The calculated band structures along high symmetry lines are shown in Figure 8a−d, while the total density of states (DOS) projected on atoms for the pure bcc-In_2O_3, pure rh-In_2O_3, 12.5% La^{3+} bcc-In_2O_3, and 12.5% La^{3+} rh-In_2O_3 are presented in Figure 8e−h, respectively. The analysis of the band structures indicates that pure bcc- and rh-In_2O_3 phases present similar and indirect band gap energy (3.74 and 3.76 eV, respectively). The doping of La^{3+} cations in the In_2O_3 matrix provides an increase in the indirect gap energy, which was the same behavior as that verified experimentally. This enhancement can be sensed more in rh-In_2O_3 (up to 4.11 eV) than in bcc-In_2O_3 (up to 3.82 eV) doped structures, due to the increase in electron density caused by the dopant.[75]

The DOS of pure bcc- and rh-In_2O_3 phases (Figure 8e,f, respectively) indicates that the upper part of the valence band (VB) consists mainly of 2p O orbitals, while the conduction band (CB) is mostly composed of 5p In orbitals. Doping the In_2O_3 matrix with La^{3+} resulted in a VB similar to those of both pure bcc- and rh-In_2O_3 phases. However, the CB in Figure 8h has a prevailing La 5d character, more noticeable than that in Figure 8g, showing an effective hybridization with 2p O orbitals to generate the distorted [LaO_6] clusters.

The La^{3+}-doping process for the rh-doped structure shows a strong Coulomb force between La^{3+} cations and oxygen anions

DOI: 10.1021/acs.inorgchem.9b01728
Inorg. Chem. 2019, 58, 11738−11750

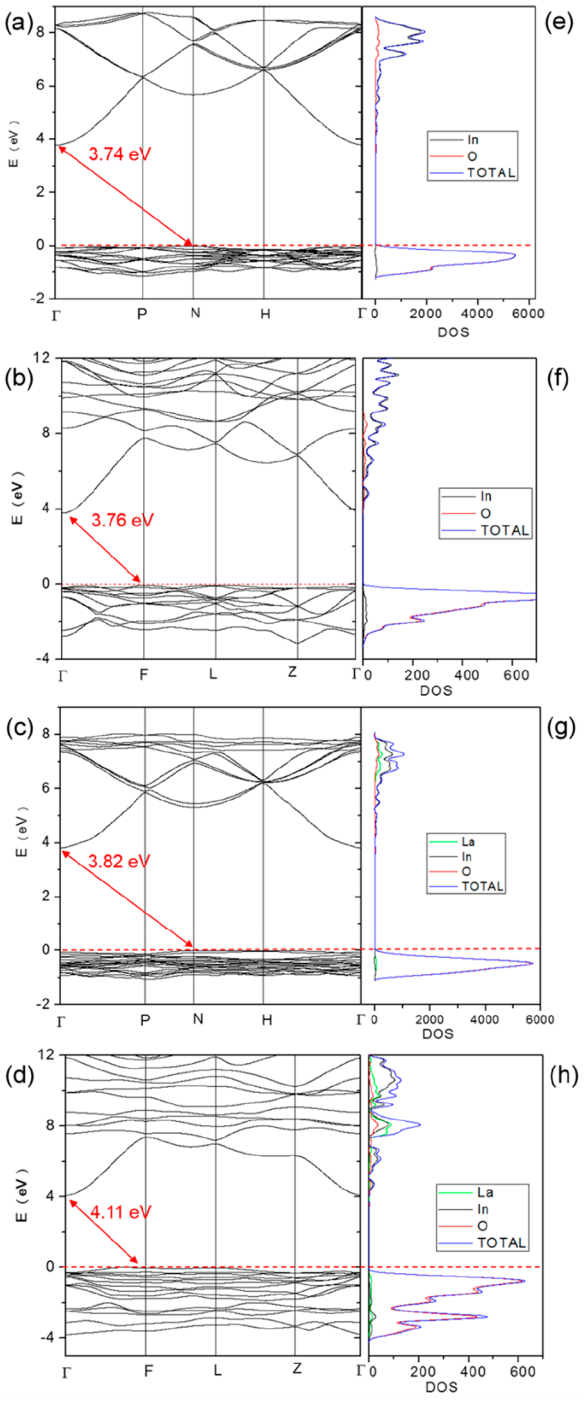

Figure 8. Band structure of bcc-In_2O_3 (a), rh-In_2O_3 (b), 12.5% La^{3+}-doped bcc-In_2O_3 (c), and 12.5% La^{3+}-doped rh-In_2O_3 (d). DOS projected on atoms for bcc-In_2O_3 (e), rh-In_2O_3 (f), 12.5% La^{3+}-doped bcc-In_2O_3 (g), and 12.5% La^{3+}-doped rh-In_2O_3 (h).

that can result in the structural rotation of the $[LaO_6]$ octahedra. This fact can increase the La−O bond length with a concomitant increment of the rotation for the octahedra in the rh phase with respect to the bcc phase, giving rise to the appearance of long-range structural disorder. This result explains the experimental observations, in which a suitable amount of La^{3+}content (12.5%) covers states in the CB of rh-In_2O_3 structure leading to a shift in the absorption to higher energies, a result known as the Burstein−Moss effect.[76] Other authors also attributed the widening of the bandgap to this effect, reporting a blueshift in the absorption edge for the In_2O_3 doped with Fe ions,[77] and He et al.[78] noticed an increase in the band gap of ZnO with the increment of the La ions content. Oxygen vacancies also contribute to carrier density, affecting the gap energy, since they generate defects between the valence band and the conduction band.[79] The existence of these vacancies is confirmed by photoluminescence spectra.

Study of the PL emissions in materials provides valuable information about aspects involving intermediate energy levels and energy transfer mechanisms. The PL emissions obtained at room temperature with λ = 350 nm are shown in Figure 9. The

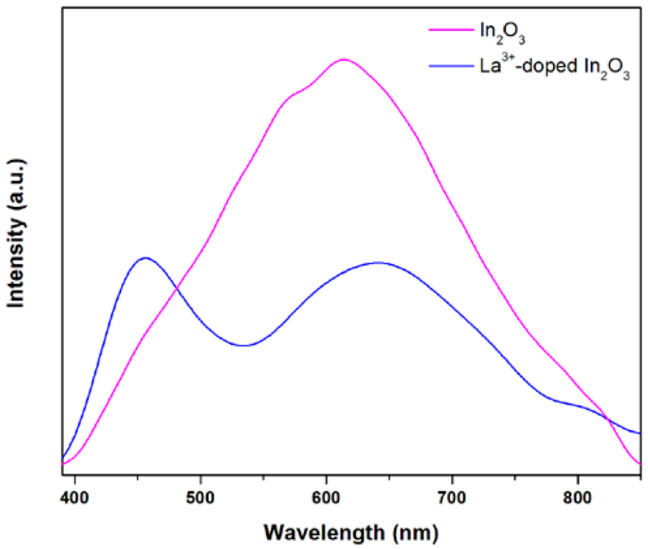

Figure 9. Photoluminescence spectra of In_2O_3 and La^{3+}-doped In_2O_3 samples.

photoluminescence of In_2O_3 nanostructures is mainly related to oxygen defects, such as oxygen vacancies and interstitial oxygen, as well as to indium vacancies. The undoped In_2O_3 sample exhibits a broad emission band centered at approximately 617 nm, while in the La^{3+}-doped In_2O_3 sample the emission band undergoes a decrease in intensity and presents an additional emission at approximately 450 nm (blue emission). Green emissions were attributed to the presence of oxygen vacancies in the bulk material, which can act as recombination centers.[80] Wu et al.[27] claimed that the blue emissions of the nanostructures of In_2O_3 can be accounted for by the radiative combination between electrons located in oxygen vacancies (V_o^x) of the donor band and holes in vacancies of indium and oxygen (V_{In}, $V_o)^x$. Yang et al.[81] demonstrated that the emission in the blue is the result of the recombination of electrons that occupy oxygen vacancies with photoexcited holes.

The PL behavior is strongly dependent on the structural modifications generated from intrinsic defects or dopant ions. Zhang et al.[39] observed an enhancement of PL emission for Gd^{3+}-doped rh-In_2O_3 nanoparticles, which was attributed to the deep level or trap state emissions. As it has been extensively reported in the literature, the insertion of La^{3+} ions in the In_2O_3 matrix produce a suppression of the PL intensity, thus endowing La^{3+} ions with the ability to prevent electron−hole recombination.[82] The different PL aspects observed for the undoped In_2O_3 and La^{3+}-doped In_2O_3 samples evidence the alternative

DOI: 10.1021/acs.inorgchem.9b01728
Inorg. Chem. 2019, 58, 11738−11750

recombination mechanism of each sample when defects, such as dopants, are introduced.

The electrochemical activity of undoped and doped In_2O_3 with 4.0 mol % La^{3+} films for water oxidation was investigated by cyclic voltammetry in 0.1 mol L^{-1} phosphate buffer, with the addition of KOH until pH 13. CV studies obtained for the ITO background are also included for comparison purposes. Figure 10 exhibits the electrocatalytic oxygen evolution reaction of

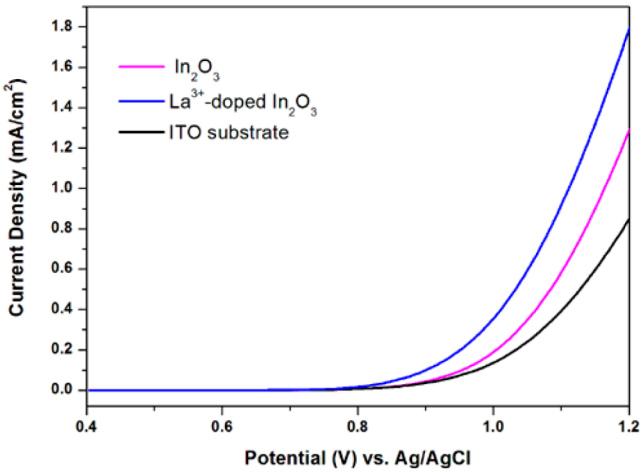

Figure 10. CVs of the ITO background, In_2O_3, and La^{3+}-doped In_2O_3 films in phosphate buffer, pH 13.

In_2O_3 films, with an onset potential of 0.80 V (vs Ag/AgCl) for In_2O_3, while for the La^{3+}-doped In_2O_3 film, this process takes place at lower potential, around 0.74 V, thus indicating a higher charge transfer kinetics.[83] In addition, the doped In_2O_3 film exhibited a higher current density when compared to the In_2O_3 film.

During the electrochemical process, the applied potential in In_2O_3 nanostructure films promotes the formation of electron−hole pairs, which are responsible for water oxidation. In this arrangement, oxygen is produced from water decomposition by holes generated in the In_2O_3 film surface, and intermediate species produced during the four-electron reaction may capture electrons from the conduction band.[6,83]

The La^{3+} doping leads to a symmetry breaking process[36,84] that can induce the formation of intermediary energy levels within the forbidden band gap and that can act as trap states reducing the electron/hole recombination rates, as observed by Liu et al.[85] and Zhou and Zhao[86] in samples containing mixed TiO_2 phases. Moreover, accordingly to Yalavarthi et al.,[87] the electron/hole recombination influences the charge transfer efficiency, and a lower recombination rate can leads to a more efficient electrochemical performance. Furthermore, an increases of the charge separation can be associated with the presence of the La empty 4f orbitals, that is able to suppress the recombination as well.[88]

The above cited factors allowed a higher electrocatalytic efficiency of O_2 evolution for La^{3+}-doped In_2O_3 films compared to the In_2O_3 sample. The Scheme 1 shows O_2 evolution bubbles on the La^{3+}-doped In_2O_3 film surface during application of 1.2 V and the respective schematic representation of electron−hole formation during this process. Oxygen vacancies are dominant defects in In_2O_3 and they are considered active sites for electrochemical processes.[89] Zhang et al.[90] provided evidence that oxygen vacancies reduce the activation energy of O−O

Scheme 1. O_2 Gas Bubbles Formed on the La^{3+}-Doped In_2O_3 Film during Application of 1.2 V and Schematic Representation of the Electron−Hole Formation

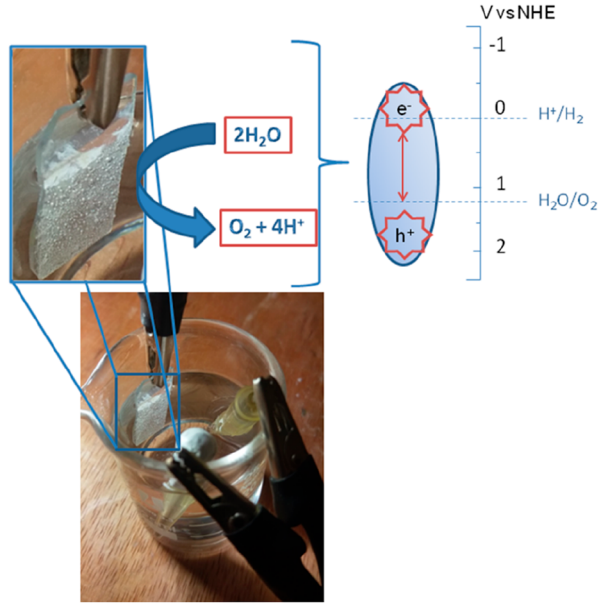

bond formation, that is, the rate-determining step for catalytic water oxidation.

The electrochemical performance in the La^{3+}-doped In_2O_3 sample is related to the bulk and surface properties resulting from the presence and the concentration of this dopant. Increasing the La amount in the In_2O_3 would not necessarily result in linear improvement of the catalytic efficiency, since aspects considered to be key factors to enhance the electrochemical activity, such as the presence of oxygen vacancies, can present a two-sided effect, being crucial to favor the electrocatalytic activation, but the excess of this oxygen defect can result in recombinative centers reducing the efficiency of the process as reported by Gan et al.[9] Therefore, the prediction of the electrochemical activity in the function of the La content constitutes a complex issue, in view of the several factors that affect the charge transfer processes in the oxide surface, being specific for each dopant amount.

These results are in accordance with the PL measurements, which exhibited a lower intensity band for the doped sample and an additional band near 450 nm, evidencing a high concentration of electron traps in La^{3+}-doped In_2O_3, assigned to oxygen vacancies. The analysis of the Raman spectra also indicated a higher number of oxygen vacancies for La^{3+}-doped In_2O_3 compared to the In_2O_3 sample. These traps are responsible for decreasing electron/hole recombination rates and, consequently, for improving the charge transfer processes in the oxide surface. Therefore, the electrochemical performance recorded from the samples indicates that the insertion of lanthanum promoted defect states that affect the charge carrier transfer process.

The influence of the pH value on the activity of In_2O_3 films for water oxidation was evaluated in order to suggest the prevailing mechanism reaction. Both undoped and doped In_2O_3 at 4.0 mol % La^{3+} samples exhibited a similar behavior in the range of pH 7.0−13.0, and the onset potential for water oxidation decreased with increasing pH values (Figure S3a,b). This pH dependence indicates a proton-coupled electron transfer (PCET) reac-

DOI: 10.1021/acs.inorgchem.9b01728
Inorg. Chem. 2019, 58, 11738−11750

tion.[4,7,91] One prevailing reaction mechanism proposed for oxides in an alkaline pH medium is the direct adsorption of OH^- molecules by the surface, forming a charged intermediate. Removing one electron and one proton from the $[(SURFACE)-OH]^-$ intermediate, the formed $[(SURFACE)-O]^-$ can interact with other H_2O molecule generating $[(SURFACE)-OOH]^-$. Another stage of deprotonation and electron transfer forms $[(SURFACE)-OO]^-$; thereafter, the loss of one electron forms $In_2O_{3(SURFACE)}-OO$ and releases the O_2 molecules with consequent recovery of the oxide surface.[4,7,92]

4. CONCLUSIONS

In_2O_3 and La^{3+}-doped In_2O_3 nanostructures were successfully synthesized by a microwave-assisted hydrothermal method followed by microwave calcination. The structures were elucidated by X-ray diffraction, which indicated the formation of the bcc-In_2O_3 structure for the undoped sample and a mixture of bcc- and rh-In_2O_3 structures for the La^{3+}-doped sample. The Rietveld refinement provided information about the effect of the doping process of La^{3+} cations in the lattice parameters of the In_2O_3 matrix and determined the proportion of bcc- and rh-In_2O_3 polymorphs obtained in La^{3+}-doped In_2O_3. The TEM images showed that the doping process of La^{3+} induces the formation of cubelike particles with a larger size when compared to the undoped In_2O_3. The Raman spectra revealed the existence of bcc- and rh-In_2O_3 for the La^{3+}-doped sample, thus corroborating the XRD results, and indicated the presence of oxygen-related defects in the materials. First-principle calculations, at the DFT level, were performed to obtain the formation energies of the undoped In_2O_3 and La^{3+}-doped In_2O_3 polymorphs, their geometry, and their electronic properties. In addition, Wulff construction was employed to match the theoretical and experimental morphologies of the cubic phase. Theoretical results indicate that for a La^{3+} substitution of 12.5%, the rh-In_2O_3 phase is more stable than the bcc-In_2O_3 phase. The structural transformation was attributed to the changes in the In−O bond lengths, O−In−O bond angles, and the electronic redistribution induced by the La^{3+}-doping process. The PL intensity decreased from undoped In_2O_3 to La^{3+}-doped In_2O_3 nanostructures, although an increase could be observed in the blue emission for the doped sample. This indicates that doping can alter the surface, generating trap states that should reduce the electron/hole recombination rates, improving the charge transfer processes, and consequently leading to a more efficient electrochemical performance.

■ ASSOCIATED CONTENT

Supporting Information

The Supporting Information is available free of charge on the ACS Publications website at DOI: 10.1021/acs.inorgchem.9b01728.

Calculated surfaces, UV−vis spectra, cyclic voltammetries, bond lengths and angles, Raman data (PDF)

■ AUTHOR INFORMATION

Corresponding Author

*E-mail: rclima@ufu.br. Tel./fax: +55-34-3239-4143.

ORCID

J. Andres: 0000-0003-0232-3957

R. C. Lima: 0000-0001-6658-7869

Present Address

L.G.: Departament de Química Física, Universitat Valencia, Burjassot, Spain.

Notes

The authors declare no competing financial interest.

■ ACKNOWLEDGMENTS

We are grateful to Coordenação de Aperfeiçoamento de Pessoal de Nível Superior (Capes), Conselho Nacional de Desenvolvimento Científico e Tecnologico (CNPq), Fundação de Amparo a Pesquisa do Estado de Minas Gerais (FAPEMIG) (APQ-00988-13), and Grupo de Materiais Inorgânicos do Triângulo (GMIT) - Research Group supported by FAPEMIG (APQ-00330-14) for the financial support. This work was partially supported by the Brazilian Institute of Science and Technology (INCT) in Carbon Nanomaterials. J.A. acknowledges financial support from Universitat Jaume I for project UJIB2016-25, Generalitat Valenciana (PrometeoII/2014/022, ACOMP/2014/270, and ACOMP/2015/1202), Ministerio de Economia y Competitividad, Spain (project CTQ2015-65207-P). I.S. also thanks the Spanish Ministerio de Economía, Industria y Competitividad for a postdoctoral "Juan de la Cierva-Incorporación" fellowship. We also acknowledge the Servei Informática, Universitat Jaume I, for a generous allotment of computer time.

■ REFERENCES

(1) Vineesh, T. V.; Mubarak, S.; Hahm, M. G.; Prabu, V.; Alwarappan, S.; Narayanan, T. N. Controllably Alloyed, Low Density, Free-standing Ni-Co and Ni-Graphene Sponges for Electrocatalytic Water Splitting. *Sci. Rep.* **2016**, *6*, 31202.

(2) Yang, J. H.; Wang, D. G.; Han, H. X.; Li, C. Roles of Cocatalysts in Photocatalysis and Photoelectrocatalysis. *Acc. Chem. Res.* **2013**, *46* (8), 1900−1909.

(3) Betley, T. A.; Wu, Q.; Van Voorhis, T.; Nocera, D. G. Electronic design criteria for O-O bond formation via metal-oxo complexes. *Inorg. Chem.* **2008**, *47* (6), 1849−1861.

(4) Huynh, M. H. V.; Meyer, T. J. Proton-coupled electron transfer. *Chem. Rev.* **2007**, *107* (11), 5004−5064.

(5) Mandal, H.; Shyamal, S.; Hajra, P.; Samanta, B.; Fageria, P.; Pande, S.; Bhattacharya, C. Improved photoelectrochemical water oxidation using wurtzite ZnO semiconductors synthesized through simple chemical bath reaction. *Electrochim. Acta* **2014**, *141*, 294−301.

(6) Peter, L. M.; Upul Wijayantha, K. G. Photoelectrochemical Water Splitting at Semiconductor Electrodes: Fundamental Problems and New Perspectives. *ChemPhysChem* **2014**, *15* (10), 1983−1995.

(7) Romeiro, F. C.; Rodrigues, M. A.; Silva, L. A. J.; Catto, A. C.; da Silva, L. F.; Longo, E.; Nossol, E.; Lima, R. C. rGO-ZnO nanocomposites for high electrocatalytic effect on water oxidation obtained by microwave-hydrothermal method. *Appl. Surf. Sci.* **2017**, *423*, 743−751.

(8) Bierwagen, O. Indium oxide-a transparent, wide-band gap semiconductor for (opto)electronic applications. *Semicond. Sci. Technol.* **2015**, *30* (2), 024001.

(9) Gan, J. Y.; Lu, X. H.; Wu, J. H.; Xie, S. L.; Zhai, T.; Yu, M. H.; Zhang, Z. S.; Mao, Y. C.; Wang, S. C. I.; Shen, Y.; Tong, Y. X. Oxygen vacancies promoting photoelectrochemical performance of In2O3 nanocubes. *Sci. Rep.* **2013**, *3*, 1021.

(10) Gu, F. B.; Li, C. J.; Han, D. M.; Wang, Z. H. Manipulating the Defect Structure (V-O) of In_2O_3 Nanoparticles for Enhancement of Formaldehyde Detection. *ACS Appl. Mater. Interfaces* **2018**, *10* (1), 933−942.

(11) Davies, D. W.; Walsh, A.; Mudd, J. J.; McConville, C. F.; Regoutz, A.; Kahk, J. M.; Payne, D. J.; Dhanak, V. R.; Hesp, D.; Pussi, K.; Lee, T. L.; Egdell, R. G.; Zhang, K. H. L. Identification of Lone-Pair Surface States on Indium Oxide. *J. Phys. Chem. C* **2019**, *123* (3), 1700−1709.

DOI: 10.1021/acs.inorgchem.9b01728
Inorg. Chem. 2019, 58, 11738−11750

(12) Park, K. W.; Kang, S. B.; Jeong, J. A.; Choi, S. W.; Kim, J.; You, I. K.; Yang, Y. S.; Kim, H. K. Liquid crystal devices incorporating transparent Zn, Sn co-doped In_2O_3 electrodes prepared by direct inkjet-printing of nanosized particles. *J. Phys. D: Appl. Phys.* **2013**, *46* (14), 145301.
(13) Ibrahim, H.; Temerk, Y. Novel sensor for sensitive electrochemical determination of luteolin based on In_2O_3 nanoparticles modified glassy carbon paste electrode. *Sens. Actuators, B* **2015**, *206*, 744−752.
(14) Temerk, Y.; Ibrahim, H. Fabrication of a novel electrochemical sensor based on Zn-In_2O_3 nanorods coated glassy carbon microspheres paste electrode for square wave voltammetric determination of neuroprotective hibifolin in biological fluids and in the flowers of hibiscus vitifolius. *J. Electroanal. Chem.* **2016**, *782*, 9−18.
(15) Munoz, A. G.; Heine, C.; Hannappel, T.; Lewerenz, H. J. Solar tandem water splitting from efficient III-V photovoltaics: Implications of electrochemical surface activation. *Electrochim. Acta* **2018**, *260*, 861−871.
(16) Zhao, Y. J.; Xie, R. J.; Dierre, B.; Takeda, T.; Sekiguchi, T.; Hirosaki, N.; Wang, L. Enhanced cathodoluminescence of green beta-sialon: Eu^{2+} phosphor by In_2O_3 coating. *J. Alloys Compd.* **2017**, *727*, 1110−1114.
(17) Chen, P.; Yin, X. T.; Que, M. D.; Yang, Y. W.; Liu, X. B.; Que, W. X. Bilayer photoanode approach for efficient In_2O_3 based planar heterojunction perovskite solar cells. *J. Alloys Compd.* **2018**, *735*, 938−944.
(18) Chava, R. K.; Cho, H. Y.; Yoon, J. M.; Yu, Y. T. Fabrication of aggregated In_2O_3 nanospheres for highly sensitive acetaldehyde gas sensors. *J. Alloys Compd.* **2019**, *772*, 834−842.
(19) Yang, W.; Feng, L.; He, S. H.; Liu, L. Y.; Liu, S. T. Density Gradient Strategy for Preparation of Broken In_2O_3 Microtubes with Remarkably Selective Detection of Triethylamine Vapor. *ACS Appl. Mater. Interfaces* **2018**, *10* (32), 27131−27140.
(20) Nagata, T. Indium oxide In_2O_3. In *Single Crystals of Electronic Materials*; Elsevier: 2019.
(21) Zhang, Z. G.; Wang, X. X.; Zhang, J.; Yu, M.; Zhang, J. C.; Zhang, H. D.; Long, Y. Z. Recent advances in 1D micro- and nanoscale indium oxide structures. *J. Alloys Compd.* **2018**, *752*, 359−375.
(22) de Boer, T.; Bekheet, M. F.; Gurlo, A.; Riedel, R.; Moewes, A. Band gap and electronic structure of cubic, rhombohedral, and orthorhombic In_2O_3 polymorphs: Experiment and theory. *Phys. Rev. B: Condens. Matter Mater. Phys.* **2016**, *93* (15), 155205.
(23) Wang, C. Y.; Cimalla, V.; Romanus, H.; Kups, T.; Ecke, G.; Stauden, T.; Ali, M.; Lebedev, V.; Pezoldt, J.; Ambacher, O. Phase selective growth and properties of rhombohedral and cubic indium oxide. *Appl. Phys. Lett.* **2006**, *89* (1), 011904.
(24) Farvid, S. S.; Dave, N.; Radovanovic, P. V. Phase-Controlled Synthesis of Colloidal In_2O_3 Nanocrystals via Size-Structure Correlation. *Chem. Mater.* **2010**, *22* (1), 9−11.
(25) Yin, J. F.; Cao, H. Q. Synthesis and Photocatalytic Activity of Single-Crystalline Hollow rh-In_2O_3 Nanocrystals. *Inorg. Chem.* **2012**, *51* (12), 6529−6536.
(26) Kock, E. M.; Kogler, M.; Zhuo, C.; Schlicker, L.; Bekheet, M. F.; Doran, A.; Gurlo, A.; Penner, S. Surface chemistry and stability of metastable corundum- type In_2O_3. *Phys. Chem. Chem. Phys.* **2017**, *19* (29), 19407−19419.
(27) Wu, M. M.; Wang, C.; Zhao, Y.; Xiao, L. S.; Zhang, C.; Yu, X. Q.; Luo, B. F.; Hu, B.; Fan, W. Q.; Shi, W. D. Hydrothermal synthesis of porous rh-In_2O_3 nanostructures with visible-light-driven photocatalytic degradation of tetracycline. *CrystEngComm* **2015**, *17* (11), 2336−2345.
(28) Li, P.; Fan, H. Q.; Cai, Y.; Xu, M. M.; Long, C. B.; Li, M. M.; Lei, S. H.; Zou, X. W. Phase transformation (cubic to rhombohedral): the effect on the NO_2 sensing performance of Zn-doped flower-like In_2O_3 structures. *RSC Adv.* **2014**, *4* (29), 15161−15170.
(29) Okte, A. N. Characterization and photocatalytic activity of Ln (La, Eu, Gd, Dy and Ho) loaded ZnO nanocatalysts. *Appl. Catal., A* **2014**, *475*, 27−39.
(30) Xu, J.; Liu, J. B.; Liu, B. X.; Li, S. N.; Wei, S. H.; Huang, B. Design of n-Type Transparent Conducting Oxides: The Case of Transition Metal Doping in In_2O_3. *Adv. Electron. Mater.* **2018**, *4* (3), 1700553.
(31) Apostolov, A. T.; Apostolova, I. N.; Wesselinowa, J. M. Theoretical study of room temperature ferromagnetism and band gap energy of pure and ion doped In_2O_3 nanoparticles. *J. Magn. Magn. Mater.* **2018**, *456*, 263−268.
(32) Ouacha, H.; Kleineberg, U.; Albrithen, H. Morphology control, electronic properties and evolution of light emission in faceted indium oxide structures. *J. Phys. D: Appl. Phys.* **2017**, *50* (45), 455102.
(33) Farvid, S. S.; Hegde, M.; Radovanovic, P. V. Influence of the Host Lattice Electronic Structure on Dilute Magnetic Interactions in Polymorphic Cr(III)-Doped In_2O_3 Nanocrystals. *Chem. Mater.* **2013**, *25* (2), 233−244.
(34) Marinho, J. Z.; Montes, R. H. O.; de Moura, A. P.; Longo, E.; Varela, J. A.; Munoz, R. A. A.; Lima, R. C. Rapid preparation of alpha-FeOOH and alpha-Fe_2O_3 nanostructures by microwave heating and their application in electrochemical sensors. *Mater. Res. Bull.* **2014**, *49*, 572−576.
(35) Simoes, A. Z.; Ramirez, M. A.; Riccardi, C. S.; Longo, E.; Varela, J. A. Effect of the microwave oven on structural, morphological and electrical properties of $SrBi_4Ti_4O_{15}$ thin films grown on Pt/Ti/SiO_2/Si substrates by a soft chemical method. *Mater. Charact.* **2008**, *59* (6), 675−680.
(36) Lemos, S. C. S.; Romeiro, F. C.; de Paula, L. F.; Goncalves, R. F.; de Moura, A. P.; Ferrer, M. M.; Longo, E.; Patrocinio, A. O. T.; Lima, R. C. Effect of Er^{3+} ions on the phase formation and properties of In_2O_3 nanostructures crystallized upon microwave heating. *J. Solid State Chem.* **2017**, *249*, 58−63.
(37) Priyanka, K. P.; Revathy, V. R.; Rosmin, P.; Thrivedu, B.; Elsa, K. M.; Nimmymol, J.; Balakrishna, K. M.; Varghese, T. Influence of La doping on structural and optical properties of TiO_2 nanocrystals. *Mater. Charact.* **2016**, *113*, 144−151.
(38) Zhang, T.; Gu, F. B.; Han, D. M.; Wang, Z. H.; Guo, G. S. Synthesis, characterization and alcohol-sensing properties of rare earth doped In_2O_3 hollow spheres. *Sens. Actuators, B* **2013**, *177*, 1180−1188.
(39) Zhang, W. H.; Wang, F.; Zhang, W. D. Phase transformation of ultrathin nanowires through lanthanide doping: from InOOH to rh-In_2O_3. *Dalton Trans.* **2013**, *42* (13), 4361−4364.
(40) Keriti, Y.; Keffous, A.; Dib, K.; Djellab, S.; Trari, M. Photoluminescence and photocatalytic properties of Er^{3+}-doped In_2O_3 thin films prepared by sol-gel: application to Rhodamine B degradation under solar light. *Res. Chem. Intermed.* **2018**, *44* (3), 1537−1550.
(41) Keriti, Y.; Keffous, A.; Gabouze, N.; Trari, M. Concentration-dependent visible photoluminescence of In_2O_3:Er^{3+} under 532 nm excitation. *Optik* **2019**, *176*, 419−424.
(42) Oppong, S. O. B.; Anku, W. W.; Opoku, F.; Shukla, S. K.; Govender, P. P. Photodegradation of Eosin Yellow Dye in Water under Simulated Solar Light Irradiation Using La-Doped ZnO Nanostructure Decorated on Graphene Oxide as an Advanced Photocatalyst. *ChemistrySelect* **2018**, *3* (4), 1180−1188.
(43) Wei, D. D.; Jiang, W. H.; Gao, H. Y.; Chuai, X. H.; Liu, F. M.; Liu, F. M.; Sun, P.; Liang, X. S.; Gao, Y.; Yan, X.; Lu, G. Y. Facile synthesis of La-doped In_2O_3 hollow microspheres and enhanced hydrogen sulfide sensing characteristics. *Sens. Actuators, B* **2018**, *276*, 413−420.
(44) Romeiro, F. C.; Marinho, J. Z.; Lemos, S. C. S.; de Moura, A. P.; Freire, P. G.; da Silva, L. E.; Longo, E.; Munoz, R. A. A.; Lima, R. C. Rapid synthesis of Co, Ni co-doped ZnO nanoparticles: Optical and electrochemical properties. *J. Solid State Chem.* **2015**, *230*, 343−349.
(45) Marinho, J. Z.; Santos, L. M.; Macario, L. R.; Longo, E.; Machado, A. E. H.; Patrocinio, A. O. T.; Lima, R. C. Rapid Preparation of $(BiO)_2CO_3$ Nanosheets by Microwave-Assisted Hydrothermal Method with Promising Photocatalytic Activity Under UV-Vis Light. *J. Braz. Chem. Soc.* **2015**, *26* (3), 498−505.
(46) Kharisov, B. I. K., O, V.; Ortiz Méndez, U. Microwave hydrothermal and solvothermal processing of materials and compounds. In *The Development and Application of Microwave Heating*; Wenbin Cao, IntechOpen, 2012.

DOI: 10.1021/acs.inorgchem.9b01728
Inorg. Chem. 2019, 58, 11738−11750

(47) Kitchen, H. J.; Vallance, S. K.; Kennedy, J. L.; Tapia-Ruiz, N.; Carassiti, L.; Harrison, A.; Whittaker, A. G.; Drysdale, T. D.; Kingman, S. W.; Gregory, D. H. Modern Microwave Methods in Solid-State Inorganic Materials Chemistry: From Fundamentals to Manufacturing. *Chem. Rev.* **2014**, *114* (2), 1170−1206.
(48) Pereira, P. F. S.; Gouveia, A. F.; Assis, M.; de Oliveira, R. C.; Pinatti, I. M.; Penha, M.; Goncalves, R. F.; Gracia, L.; Andres, J.; Longo, E. $ZnWO_4$ nanocrystals: synthesis, morphology, photoluminescence and photocatalytic properties. *Phys. Chem. Chem. Phys.* **2018**, *20* (3), 1923−1937.
(49) Larson, A. C.; Von Dreele, R. B. *General Structure Analysis System (GSAS)*; Report LAUR 86−748; Los Alamos National Laboratory, 2000.
(50) Salvatierra, R. V.; Oliveira, M. M.; Zarbin, A. J. G. One-Pot Synthesis and Processing of Transparent, Conducting, and Free-standing Carbon Nanotubes/Polyaniline Composite Films. *Chem. Mater.* **2010**, *22* (18), 5222−5234.
(51) Neiva, E. G. C.; Oliveira, M. M.; Bergamini, M. F.; Marcolino, L. H.; Zarbin, A. J. G. One material, multiple functions: graphene/$Ni(OH)_2$ thin films applied in batteries, electrochromism and sensors. *Sci. Rep.* **2016**, *6*, 33806.
(52) Dovesi, R.; Saunders, V. R.; Roetti, C.; Orlando, C. M.; Zicovich-Wilson, C. M.; Pascale, F.; Civalleri, B.; Doll, K.; Harrison, N. M.; Bush, I. J.; D'Arco, P.; Llunell, M.; Causà, M., Noël, Y.; Maschio, L.; Erba, A.; Rerat, M.; Casassa, S. *CRYSTAL17*; University of Torino, 2017.
(53) Bredow, T.; Jug, K.; Evarestov, R. A. Electronic and magnetic structure of $ScMnO_3$. *Phys. Status Solidi B* **2006**, *243* (2), R10−R12.
(54) Causa, M.; Dovesi, R.; Roetti, C. Pseudopotential hartree-fock study of 17 iii-v-semiconductors and iv-iv-semiconductors. *Phys. Rev. B: Condens. Matter Mater. Phys.* **1991**, *43* (14), 11937−11943.
(55) Wulff, G. XXV. Zur Frage der Geschwindigkeit des Wachstums und der Aufl€osung der Krystallfl€achen. *Z. Kristallogr. - Cryst. Mater.* **1901**, *34*, 449−530.
(56) Andres, J.; Gracia, L.; Gouveia, A. F.; Ferrer, M. M.; Longo, E. Effects of surface stability on the morphological transformation of metals and metal oxides as investigated by first-principles calculations. *Nanotechnology* **2015**, *26* (40), 405703.
(57) Gouveia, A. F.; Ferrer, M. M.; Sambrano, J. R.; Andres, J.; Longo, E. Modeling the atomic-scale structure, stability, and morphological transformations in the tetragonal phase of $LaVO_4$. *Chem. Phys. Lett.* **2016**, *660*, 87−92.
(58) Oliveira, M. C.; Gracia, L.; Nogueira, I. C.; Gurgel, M. F. C.; Mercury, J. M. R.; Longo, E.; Andres, J. On the morphology of $BaMoO_4$ crystals: A theoretical and experimental approach. *Cryst. Res. Technol.* **2016**, *51* (10), 634−644.
(59) Bomio, M. R. D.; Tranquilin, R. L.; Motta, F. V.; Paskocimas, C. A.; Nascimento, R. M.; Gracia, L.; Andres, J.; Longo, E. Toward Understanding the Photocatalytic Activity of $PbMoO_4$ Powders with Predominant (111), (100), (011), and (110) Facets. A Combined Experimental and Theoretical Study. *J. Phys. Chem. C* **2013**, *117* (41), 21382−21395.
(60) Longo, V. M.; Gracia, L.; Stroppa, D. G.; Cavalcante, L. S.; Orlandi, M.; Ramirez, A. J.; Leite, E. R.; Andres, J.; Beltran, A.; Varela, J. A.; Longo, E. A Joint Experimental and Theoretical Study on the Nanomorphology of $CaWO_4$ Crystals. *J. Phys. Chem. C* **2011**, *115* (41), 20113−20119.
(61) Botelho, G.; Andres, J.; Gracia, L.; Matos, L. S.; Longo, E. Photoluminescence and Photocatalytic Properties of Ag_3PO_4 Microcrystals: An Experimental and Theoretical Investigation. *ChemPlusChem* **2016**, *81* (2), 202−212.
(62) Fabbro, M. T.; Saliby, C.; Rios, L. R.; La Porta, F. A.; Gracia, L.; Li, M. S.; Andres, J.; Santos, L. P. S.; Longo, E. Identifying and rationalizing the morphological, structural, and optical properties of beta-Ag_2MoO_4 microcrystals, and the formation process of Ag nanoparticles on their surfaces: combining experimental data and first-principles calculations. *Sci. Technol. Adv. Mater.* **2015**, *16* (6), 065002.
(63) Silva, G. S.; Gracia, L.; Fabbro, M. T.; Serejo dos Santos, L. P.; Beltran-Mir, H.; Cordoncillo, E.; Longo, E.; Andres, J. Theoretical and Experimental Insight on Ag_2CrO_4 Microcrystals: Synthesis, Characterization, and Photoluminescence Properties. *Inorg. Chem.* **2016**, *55* (17), 8961−8970.
(64) Oliveira, M. C.; Gracia, L.; Nogueira, I. C.; Carmo Gurgel, M. F. d.; Mercury, J. M. R.; Longo, E.; Andres, J. Synthesis and morphological transformation of BaWO4 crystals: Experimental and theoretical insights. *Ceram. Int.* **2016**, *42* (9), 10913−10921.
(65) Wang, F.; Han, Y.; Lim, C. S.; Lu, Y. H.; Wang, J.; Xu, J.; Chen, H. Y.; Zhang, C.; Hong, M. H.; Liu, X. G. Simultaneous phase and size control of upconversion nanocrystals through lanthanide doping. *Nature* **2010**, *463* (7284), 1061−1065.
(66) Tang, Q.; Zhou, W. J.; Zhang, W.; Ou, S. M.; Jiang, K.; Yu, W. C.; Qian, Y. T. Size-controllable growth of single crystal $In(OH)_3$ and In_2O_3 nanocubes. *Cryst. Growth Des.* **2005**, *5* (1), 147−150.
(67) Cho, S. H.; Ghosh, S.; Berkson, Z. J.; Hachtel, J. A.; Shi, J.; Zhao, X.; Reimnitz, L. C.; Dahlman, C. J.; Ho, Y.; Yang, A.; Liu, Y.; Idrobo, J. C.; Chmelka, B. F.; Milliron, D. J. Syntheses of Colloidal F:In_2O_3 Cubes: Fluorine-Induced Faceting and Infrared Plasmonic Response. *Chem. Mater.* **2019**, *31* (7), 2661−2676.
(68) White, W. B.; Keramidas, V. G. VIBRATIONAL-SPECTRA OF OXIDES WITH C-TYPE RARE-EARTH OXIDE STRUCTURE. *Spectrochim. Acta A Mol. Spectrosc.* **1972**, *28* (3), 501−509.
(69) Kranert, C.; Schmidt-Grund, R.; Grundmann, M. Raman active phonon modes of cubic In_2O_3. *Phys. Status Solidi RRL* **2014**, *8* (6), 554−559.
(70) Wang, C. Y.; Dai, Y.; Pezoldt, J.; Lu, B.; Kups, T.; Cimalla, V.; Ambacher, O. Phase stabilization and phonon properties of single crystalline rhombohedral indium oxide. *Cryst. Growth Des.* **2008**, *8* (4), 1257−1260.
(71) Cao, H. M.; Xing, P. F.; Yao, D. S.; Wu, P. Annealing temperature dependent non-monotonic d(0) ferromagnetism in pristine In_2O_3 nanoparticles. *J. Magn. Magn. Mater.* **2017**, *429*, 69−73.
(72) Khan, G. G.; Ghosh, S.; Sarkar, A.; Mandal, G.; Mukherjee, G. D.; Manju, U.; Banu, N.; Dev, B. N. Defect engineered d(0) ferromagnetism in tin-doped indium oxide nanostructures and nanocrystalline thin-films. *J. Appl. Phys.* **2015**, *118* (7), 074303.
(73) Anand, K.; Kaur, J.; Singh, R. C.; Thangaraj, R. Structural, optical and gas sensing properties of pure and Mn-doped In_2O_3 nanoparticles. *Ceram. Int.* **2016**, *42* (9), 10957−10966.
(74) Kubelka, P.; Munk, F. Ein Beitrag Zur Optik Der Farbanstriche. *Z. Technol. Phys.* **1931**, *12*, 593−601.
(75) Feneberg, M.; Nixdorf, J.; Lidig, C.; Goldhahn, R.; Galazka, Z.; Bierwagen, O.; Speck, J. S. Many-electron effects on the dielectric function of cubic In_2O_3: Effective electron mass, band nonparabolicity, band gap renormalization, and Burstein-Moss shift. *Phys. Rev. B: Condens. Matter Mater. Phys.* **2016**, *93* (4), 045203.
(76) Moss, T. S. The interpretation of the properties of indium antimonide. *Proc. Phys. Soc., London, Sect. B* **1954**, *67* (418), 775−782.
(77) Jiang, F. X.; Chen, D.; Zhou, G. W.; Wang, Y. N.; Xu, X. H. The dramatic enhancement of ferromagnetism and band gap in Fe-doped In_2O_3 nanodot arrays. *Sci. Rep.* **2018**, *8*, 2417.
(78) He, H. Y.; Huang, J. F.; Fei, J.; Lu, J. La-doping content effect on the optical and electrical properties of La-doped ZnO thin films. *J. Mater. Sci.: Mater. Electron.* **2015**, *26* (2), 1205−1211.
(79) Patel, S. K. S.; Dewangan, K.; Srivastav, S. K.; Gajbhiye, N. S. Synthesis of monodisperse In_2O_3 nanoparticles and their d(0) ferromagnetism. *Curr. Appl. Phys.* **2014**, *14* (6), 905−908.
(80) Perez-Sanchez, G. F.; Chavez, E.; Cortes-Salinas, D.; Zaca-Moran, P.; Morales-Acevedo, A.; Pena-Sierra, R.; Goiz, O.; Huerta, A. T. Synthesis of In-In_2O_3 microstructures by close-spaced vapor transport (CSVT) and their transformation to In_2O_3 nanobelts at low temperature. *Vacuum* **2014**, *107*, 236−241.
(81) Yang, J.; Lin, C. K.; Wang, Z. L.; Lin, J. $In(OH)_3$ and In_2O_3 nanorod bundles and spheres: Microemulsion-mediated hydrothermal synthesis and luminescence properties. *Inorg. Chem.* **2006**, *45* (22), 8973−8979.
(82) Tahir, M. La-modified TiO_2/carbon nanotubes assembly nanocomposite for efficient photocatalytic hydrogen evolution from

DOI: 10.1021/acs.inorgchem.9b01728
Inorg. Chem. 2019, 58, 11738−11750

glycerol-water mixture. *Int. J. Hydrogen Energy* **2019**, *44* (7), 3711−3725.
(83) Bertoluzzi, L.; Lopez-Varo, P.; Jimenez Tejada, J. A.; Bisquert, J. Charge transfer processes at the semiconductor/electrolyte interface for solar fuel production: insight from impedance spectroscopy. *J. Mater. Chem. A* **2016**, *4* (8), 2873−2879.
(84) Lima, R. C.; Macario, L. R.; Espinosa, J. W. M.; Longo, V. M.; Erlo, R.; Marana, N. L.; Sambrano, J. R.; dos Santos, M. L.; Moura, A. P.; Pizani, P. S.; Andres, J.; Longo, E.; Varela, J. A. Toward an understanding of intermediate- and short-range defects in ZnO single crystals. A combined experimental and theoretical study. *J. Phys. Chem. A* **2008**, *112* (38), 8970−8978.
(85) Liu, R. D.; Li, H.; Duan, L. B.; Shen, H.; Zhang, Q.; Zhao, X. R. Influences of annealing atmosphere on phase transition temperature, optical properties and photocatalytic activities of TiO_2 phase-junction microspheres. *J. Alloys Compd.* **2019**, *789*, 1015−1021.
(86) Zhou, Y. D.; Zhao, Z. Y. Interfacial structure and properties of TiO_2 phase junction studied by DFT calculations. *Appl. Surf. Sci.* **2019**, *485*, 8−21.
(87) Yalavarthi, R.; Naldoni, A.; Kment, S.; Mascaretti, L.; Kmentova, H.; Tomanec, O.; Schmuki, P.; Zboril, R. Radiative and Non-Radiative Recombination Pathways in Mixed-Phase TiO_2 Nanotubes for PEC Water-Splitting. *Catalysts* **2019**, *9*, 204.
(88) Ako, R. T.; Ekanayake, P.; Tan, A. L.; Young, D. J. La modified TiO_2 photoanode and its effect on DSSC performance: A comparative study of doping and surface treatment on deep and surface charge trapping. *Mater. Chem. Phys.* **2016**, *172*, 105−112.
(89) Lv, X. W.; Tao, L. M.; Cao, M. L.; Xiao, X.; Wang, M. K.; Shen, Y. Enhancing photoelectrochemical water oxidation efficiency via self-catalyzed oxygen evolution: A case study on TiO_2. *Nano Energy* **2018**, *44*, 411−418.
(90) Zhang, Y.-C.; Liu, Y.-K.; Zhang, L.; E, X.-t.-f.; Pan, L.; Zhang, X.; Fazal-e-Aleem; Zou, D.-R.; Liu, S.-H.; Zou, J.-J. DFT study on water oxidation on nitrogen-doped ceria oxide. *Appl. Surf. Sci.* **2018**, *452*, 423−428.
(91) Lei, H. T.; Han, A.; Li, F. W.; Zhang, M. N.; Han, Y. Z.; Du, P. W.; Lai, W. Z.; Cao, R. Electrochemical, spectroscopic and theoretical studies of a simple bifunctional cobalt corrole catalyst for oxygen evolution and hydrogen production. *Phys. Chem. Chem. Phys.* **2014**, *16* (5), 1883−1893.
(92) Giordano, L.; Han, B. H.; Risch, M.; Hong, W. T.; Rao, R. R.; Stoerzinger, K. A.; Shao-Horn, Y. pH dependence of OER activity of oxides: Current and future perspectives. *Catal. Today* **2016**, *262*, 2−10.

DOI: 10.1021/acs.inorgchem.9b01728
Inorg. Chem. 2019, 58, 11738−11750